Research Square

Preprints are preliminary reports that have not undergone peer review.
They should not be considered conclusive, used to inform clinical practice,
or referenced by the media as validated information.

Palmitoylation-associated molecular states implicate FNDC3B in tumor progression and macrophage-associated microenvironmental remodeling in pancreatic cancer

Jiayu Liu
Peking University First Hospital
Enkui Zhang
Peking University First Hospital
Weikang Liu
Peking University First Hospital
Guangnian Liu
Peking University First Hospital
Fusheng Zhang
Peking University First Hospital
Cuixia Zhang
Peking University First Hospital
Yongqi Deng
Peking University First Hospital
Yinmo Yang
Peking University First Hospital
Yongsu Ma
Peking University First Hospital
Xiaodong Tian
tianxiaodong@pkufh.com

Peking University First Hospital

Research Article

Keywords: Pancreatic ductal adenocarcinoma, Prognosis, Palmitoylation, FNDC3B, Tumor-associated macrophages

Posted Date: October 27th, 2026

DOI: https://doi.org/10.21203/rs.3.rs-11101218/v1

License: This work is licensed under a Creative Commons Attribution 4.0 International License.
Read Full License

Additional Declarations: No competing interests reported.

Abstract

Background

Pancreatic ductal adenocarcinoma (PDAC) shows marked clinical heterogeneity and extensive tumor microenvironment (TME) remodeling. Protein palmitoylation regulates membrane-associated signaling and tumor-related biological processes, but its transcriptional relevance to PDAC molecular stratification and microenvironmental states remains unclear.

Methods

Integrated GEO and TCGA transcriptomic cohorts were used to characterize palmitoylation-related expression patterns in PDAC. Consensus clustering, ssGSEA, pathway analysis, immune infiltration estimation, and LASSO-Cox regression were applied to define molecular subtypes, construct a palmitoylation score, and develop a prognostic model. scRNA-seq, CellChat analysis, multiplex immunofluorescence, in vitro assays, western blotting, and xenograft models were used to investigate the cellular context and biological role of FNDC3B.

Results

Palmitoylation-related genes stratified PDAC patients into three molecular subtypes with distinct survival outcomes and biological programs. Cluster B showed the poorest prognosis and was enriched for proliferative, DNA repair, epithelial-mesenchymal transition, and TME-remodeling features. A patient-level palmitoylation score captured adverse subtype-associated transcriptional patterns and was associated with shorter overall survival. A five-gene prognostic model comprising FNDC3B, ALDH9A1, CAPRIN2, TTC9, and GPR133 robustly stratified patient survival across validation cohorts. FNDC3B was associated with unfavorable prognosis and macrophage-enriched immune infiltration. Functionally, FNDC3B knockdown impaired PDAC cell proliferation, colony formation, migration, and xenograft tumor growth, accompanied by reduced mTOR pathway phosphorylation. Single-cell and spatial analyses identified tumor-enriched FNDC3B-positive macrophages linked to adverse prognosis, an SPP1-centered communication program, and SPP1-rich tumor niches.

Conclusions

This study defines a palmitoylation-associated transcriptional framework for PDAC stratification and prognostic assessment. FNDC3B emerges as a risk-associated molecule linking tumor-cell malignant phenotypes, mTOR-related signaling, macrophage-enriched immune features, and spatial microenvironmental remodeling.

Background

Pancreatic ductal adenocarcinoma (PDAC) remains a clinically refractory malignancy of the digestive system, with a 5-year relative survival rate below 15%[1, 2]. Late clinical presentation, early dissemination and frequent diagnosis at locally advanced or metastatic stages continue to limit the curative impact of surgery and systemic therapy[2]. Although surgical resection, multi-agent chemotherapy and perioperative treatment strategies have improved outcomes in selected patients, recurrence, therapeutic resistance and disease progression remain major barriers in PDAC management[2–4]. Immune checkpoint blockade has changed treatment paradigms in several solid tumors, but its activity in unselected PDAC remains limited[5, 6], largely owing to low immunogenicity, desmoplastic stroma and immunosuppressive cellular infiltration[6, 7]. These observations support the need for molecular stratification frameworks that incorporate both tumor-cell programs and microenvironmental context. The clinical heterogeneity of PDAC is closely linked to molecular diversity and organization of the tumor microenvironment (TME). Transcriptomic and multi-omic studies have shown that PDAC comprises tumor-cell-intrinsic states, including classical and basal-like/squamous programs, as well as stroma-associated subtypes with prognostic relevance[8–10]. Desmoplastic stroma and an immunosuppressive ecosystem are core features of the PDAC TME and can influence disease progression by restricting drug delivery, impairing effector immune-cell infiltration and facilitating therapeutic resistance[7, 11, 12]. Tumor-associated macrophages are particularly abundant in PDAC and have been implicated in tumor progression, immune suppression, extracellular matrix remodeling and therapeutic resistance[13]. Thus, prognostic differences in PDAC should be interpreted not only through individual driver genes or isolated tumor-cell states, but also through the co-evolution of malignant epithelial programs and microenvironmental ecosystems.

Existing molecular classifications and prognostic models have improved the description of PDAC heterogeneity[8–10]. However, how post-translational regulatory mechanisms shape tumor-cell state transitions and microenvironmental adaptation remains less well defined. Protein post-translational modifications (PTMs) provide a regulatory layer between gene expression and protein function by affecting protein localization, stability, trafficking and signaling output[14]. Among these PTMs, S-palmitoylation is a dynamic and reversible lipid modification that attaches palmitate to cysteine residues and regulates membrane association, intracellular trafficking, protein complex assembly and membrane-proximal signaling[15–17]. Because many receptors, adhesion molecules, immune-regulatory proteins and signaling intermediates depend on membrane localization and trafficking, palmitoylation may influence not only tumor-cell proliferation and survival but also cell-cell communication within the TME[18]. In cancer, palmitoylation dysregulation has been implicated in oncogenic signaling, metabolic adaptation, invasion, therapy resistance and immune escape[19]. PDAC-related studies have linked palmitoylation dysregulation to tumorigenesis and radiosensitivity[20], MYC-driven tumor progression[21], glycolytic activity and chemotherapy response[22], and macrophage-phagocytosis evasion[23]. However, most studies have focused on individual palmitoylating enzymes, substrates or signaling axes. Whether coordinated palmitoylation-associated transcriptional heterogeneity can define

clinically meaningful PDAC subtypes and connect tumor-cell programs with macrophage-associated TME remodeling remains insufficiently clarified.

Here, we systematically interrogated palmitoylation-related gene expression patterns in PDAC to identify molecular subtypes, derive a patient-level palmitoylation score and develop a prognostic risk model. Rather than treating palmitoylation-related genes solely as isolated enzymes or substrates, we used their coordinated expression patterns as a transcriptional entry point into PDAC heterogeneity. FNDC3B was subsequently prioritized as a risk-associated candidate gene, and multi-level analyses were integrated to characterize its cellular distribution, biological role and relationship with immune microenvironmental remodeling. A workflow diagram is provided to summarize the study design **(Fig. 1)**. This integrated analysis provides a palmitoylation-associated framework for PDAC molecular stratification, prognostic assessment and investigation of tumor-immune interactions.

Materials and Methods

Bulk RNA sequencing data acquisition and preprocessing

Bulk transcriptomic profiles and corresponding clinical information for pancreatic ductal adenocarcinoma (PDAC) were obtained from the Gene Expression Omnibus (GEO) and The Cancer Genome Atlas (TCGA) databases[24, 25]. The GSE62452 and GSE85916 datasets were integrated as the primary GEO-meta cohort for subtype discovery, palmitoylation score construction and model development. Additional GEO datasets, including GSE21501, GSE57495 and GSE28735, together with TCGA-PAAD, were used for cohort-level robustness assessment, external validation and combined-cohort analyses of the prognostic model and key genes. The IMvigor210 cohort was included for exploratory immunotherapy-response analysis[26]. Samples lacking essential survival information were excluded from survival analyses. Expression matrices were log2-transformed when required and normalized using the limma R package[27]. Batch effects across datasets were corrected using the ComBat algorithm implemented in the sva package[28], followed by Z-score normalization for cross-cohort analyses.

Identification of palmitoylation-related genes

Palmitoylation-related genes were retrieved from the Molecular Signatures Database (MSigDB; v2025.1, Homo sapiens)[29]. Gene Ontology (GO) terms related to protein palmitoylation and depalmitoylation were used to define the candidate gene set[30]. A total of 40 candidate genes were initially identified. After matching gene symbols with the integrated transcriptomic matrix, 34 genes with available expression data were retained for subsequent analyses.

Consensus clustering analysis

Unsupervised consensus clustering was performed using the ConsensusClusterPlus R package[31] based on the expression profiles of palmitoylation-related genes in the primary GEO-meta cohort. Clustering was repeated 1,000 times with 80% sample resampling, using Pearson correlation distance and hierarchical clustering. The optimal cluster number was determined according to the consensus cumulative distribution function (CDF), delta area curve, and consensus matrix. Principal component analysis (PCA) was used to visualize clustering patterns.

Construction of the palmitoylation score

A palmitoylation score (PalS) was calculated using single-sample gene set enrichment analysis (ssGSEA) implemented in the GSVA R package (version 2.4.8; R version 4.5.2)[32, 33]. The scoring gene set consisted of prognosis-related genes identified by univariate Cox regression among the overlapping subtype-associated differentially expressed genes (DEGs). Patients were stratified into PalS_High and PalS_Low groups according to the median PalS value.

Construction of the prognostic model using iterative LASSO-Cox regression

A palmitoylation-associated prognostic signature was developed from survival-associated candidate genes using an iterative LASSO-Cox regression approach[34]. In each iteration, 80% of samples were randomly resampled with replacement and subjected to 10-fold cross-validated LASSO-Cox regression using the lambda.min criterion. Genes with non-zero coefficients were recorded in each iteration. This procedure was repeated 1,000 times, and genes selected in at least 50 iterations were retained as stable candidates and ranked according to selection frequency. Cox models containing increasing numbers of top-ranked genes were evaluated using the mean time-dependent area under the curve (AUC) for 1-, 2- and 3-year overall survival[35]. Because the predictive performance increased rapidly up to the five-gene model and then reached a plateau with only marginal improvement after adding more genes, a parsimonious five-gene signature was retained for downstream validation. The risk score was calculated as the sum of gene expression values weighted by multivariate Cox regression coefficients.

Differential expression and functional enrichment analyses

Pairwise differential expression analyses among palmitoylation-related molecular subtypes were performed using the limma R package[27]. Overlapping subtype-associated differentially expressed genes (DEGs) were defined as genes shared across all three pairwise subtype comparisons. Prognosis-associated overlapping genes were identified by univariate Cox regression analysis. GO enrichment analysis was performed using the clusterProfiler R package[36].

Gene set variation analysis (GSVA) was performed using hallmark and curated pathway gene sets[33], and differential pathway activity between groups was estimated using the limma package[27]. For

pathway-level visualization, gene sets with significant differences between comparison groups were retained. Immune-cell infiltration was estimated using the CIBERSORT algorithm with the LM22 signature matrix[37]. Correlation matrices and scatter plots were used to visualize associations among model genes, immune-cell infiltration and palmitoylation-related genes.

Single-cell RNA sequencing analysis

The GSE212966 single-cell RNA sequencing (scRNA-seq) dataset, comprising paired tumor and adjacent pancreatic tissue samples from six PDAC patients, was obtained from a previously published study[38]. For the main single-cell analyses, only tumor-derived samples were retained. Adjacent samples were incorporated only for paired tumor–adjacent comparisons of FNDC3B expression and FNDC3B-positive macrophage distribution. Data processing was performed using the Seurat R package[39]. Cells with fewer than 500 detected genes, fewer than 1,500 UMIs, mitochondrial RNA percentage ≥ 15%, or erythroid-associated signal ≥ 1% were excluded. After LogNormalize normalization, the top 2,000 variable features were selected, and samples were integrated using the Seurat anchor-based workflow with FindIntegrationAnchors and IntegrateData. PCA and uniform manifold approximation and projection (UMAP)[40] were used for dimensionality reduction and visualization, followed by graph-based clustering. Cell types were annotated using canonical marker genes and established PDAC single-cell annotation strategies. Palmitoylation-associated transcriptional activity at the single-cell level was quantified using AUCell[41].

Cell-cell communication analysis

Cell-cell communication analysis was performed using the CellChat R package based on curated ligand–receptor interactions[42]. Annotated cell populations were used as input groups. FNDC3B-positive macrophages were defined as macrophages with normalized FNDC3B expression > 0 after log-normalization, whereas macrophages with no detectable FNDC3B expression were defined as FNDC3B-negative macrophages. Communication probabilities and pathway-level signaling networks were inferred across cell populations. Outgoing signaling patterns from FNDC3B-positive and FNDC3B-negative macrophages were compared, and dominant signaling pathways and ligand–receptor pairs were further examined.

Cell culture and lentiviral transduction

Human pancreatic cancer cell lines PANC-1, PaTu8988, MiaPaCa-2, AsPC-1, BxPC-3 and Capan-1 were obtained from the American Type Culture Collection (ATCC). Cells were cultured in DMEM (Gibco, USA) supplemented with 10% fetal bovine serum (Gibco, USA) and 1% penicillin–streptomycin solution (Gibco, USA) at 37°C in a humidified incubator with 5% CO_2. To establish stable FNDC3B-knockdown pancreatic cancer cells, lentiviral vectors carrying short hairpin RNAs targeting human FNDC3B and the corresponding negative control vector were obtained from GeneChem (Shanghai, China). The shRNA

sequences were cloned into the GV493 lentiviral vector carrying the hU6-MCS-CBh-gcGFP-IRES-puromycin cassette, and the recombinant vectors were confirmed by Sanger sequencing. For lentivirus production, recombinant lentiviral vectors were co-transfected with the packaging plasmids psPAX2 and pMD2.G into 293T cells using Lipofectamine 2000 reagent (Invitrogen; Thermo Fisher Scientific, USA). Lentiviral particles were harvested 72 h after transfection, centrifuged to remove cell debris, filtered through 0.45 μm cellulose acetate filters and stored at − 80°C until use. PANC-1 and PaTu8988 cells were transduced with lentivirus and selected with puromycin to generate stable FNDC3B-knockdown cells.

The shRNA sequences used for FNDC3B knockdown were as follows: shFNDC3B-1, CGGATCTGAAATCCTTGCTTA; shFNDC3B-2, GCCATCATTGTGCTTGGCTTT; and shNC, TTCTCCGAACGTGTCACGT.

Cell proliferation and colony formation assays

For CCK-8 assays, pancreatic cancer cells were seeded into 96-well plates at a density of 4,000 cells per well, with five replicate wells for each condition. Cell viability was measured daily for five consecutive days. At each time point, 10 μL of CCK-8 solution was added to each well and incubated for 1 h at 37°C, and absorbance was measured at 450 nm.

For colony formation assays, 1,000 cells were seeded into six-well plates with three replicate wells per group and cultured for 14 days. Colonies were fixed with paraformaldehyde and stained with crystal violet (Solarbio, #G1062, China), followed by imaging and quantification.

Transwell migration assay

A total of 1 × 10^5 pancreatic cancer cells suspended in 200 μL serum-free medium were seeded into the upper chambers of Transwell inserts with 8.0-μm pores (Corning, USA), and 600 μL of complete medium containing 10% FBS was added to the lower chambers as a chemoattractant. After 24 h of incubation, cells remaining on the upper membrane surface were removed with cotton swabs. Migrated cells on the lower surface were fixed with paraformaldehyde, stained with crystal violet, photographed, and quantified. All experiments were performed independently in triplicate.

Western blotting

Cells were washed with PBS and lysed on ice in RIPA buffer (Solarbio, Beijing, China) supplemented with PMSF and phosphatase inhibitor cocktail. Protein lysates were centrifuged at 12,000 × g for 15 min at 4°C, and protein concentrations were determined using a BCA protein assay kit. Equal amounts of protein were separated by SDS–PAGE and transferred onto 0.22-μm PVDF membranes (Millipore, USA). Membranes were blocked with 5% bovine serum albumin for 1 h at room temperature and incubated overnight at 4°C with primary antibodies. After washing with TBST, membranes were incubated with HRP-conjugated secondary antibodies for 1 h at room temperature. Protein bands were visualized using enhanced chemiluminescence reagents. The primary antibodies used were as follows: FNDC3B (Proteintech, #86272-1-RR, 1:10000), β-actin (Proteintech, #66009-1-Ig, 1:50000), mTOR (Cell Signaling

Technology, #2983, 1:1000), p-mTOR (Ser2448) (Cell Signaling Technology, #5536, 1:1000), S6 (Cell Signaling Technology, #2217, 1:1000), p-S6 (Ser235/236) (Cell Signaling Technology, #4858, 1:2000), 4E-BP1 (Cell Signaling Technology, #9644, 1:1000), and p-4E-BP1 (Thr37/46) (Cell Signaling Technology, #2855, 1:1000).

Flow cytometry

Cell-cycle distribution was analyzed using the Cell Cycle and Apoptosis Analysis Kit (C1052, Beyotime Biotechnology, China) according to the manufacturer's instructions. Briefly, cells were fixed in 70% ethanol at 4°C and stained with propidium iodide (PI)/RNase staining solution in the dark. Samples were analyzed by flow cytometry (BD Biosciences, USA), and data were processed using FlowJo software (v10).

Multiplex immunofluorescence staining

Multiplex immunofluorescence (mIF) staining was performed on formalin-fixed, paraffin-embedded tissue microarrays (TMAs) containing paired PDAC tumor and peritumoral tissue cores. TMA sections were deparaffinized, rehydrated, treated with 3% hydrogen peroxide, subjected to heat-induced antigen retrieval and blocked with 5% bovine serum albumin. A five-marker panel including panCK, CD68, FNDC3B, SPP1 and α-SMA was stained using a tyramide signal amplification-based sequential protocol. In each cycle, sections were incubated with the indicated primary antibody, followed by HRP-conjugated secondary antibody incubation, tyramide fluorophore development and antibody stripping before the next staining round. After all markers were labeled, nuclei were counterstained with DAPI, and sections were mounted with anti-fade mounting medium. Fluorescence images of TMA cores were acquired using identical imaging settings for paired tumor and peritumoral tissues.

Quantitative pathology

Quantitative analysis of mIF images was performed using QuPath software (v0.6.0)[43]. Scanned TMA images were imported into QuPath, and individual tissue cores were manually annotated. Cell segmentation was performed using the Cellpose extension with a Cellpose-SAM model, with DAPI used for nuclear detection[44]. Fluorescence intensity measurements for panCK, CD68, FNDC3B, SPP1 and α-SMA were extracted for each detected cell. Marker-positive cells were defined using optimized single-measurement classifiers based on marker-specific fluorescence intensity. Composite classifiers were generated to identify FNDC3B-negative CD68-positive and FNDC3B-positive CD68-positive macrophages, and SPP1 positivity was quantified within each FNDC3B-positive or FNDC3B-negative macrophage subset. Spatial proximity analysis was performed to quantify macrophage subsets located within 30 μm of panCK-positive tumor regions or SPP1-positive cells. Correlations between the proportions of FNDC3B-positive macrophages and SPP1-positive macrophages were assessed.

Xenograft model

Five-week-old male BALB/c nude mice were housed under specific pathogen-free conditions. All animal experiments were approved by the Animal Care and Use Committee of Peking University First Hospital

(Ethical Review NO.S2025396). Control and FNDC3B-knockdown PANC-1 and PaTu8988 cells were harvested, washed with PBS, and resuspended in PBS at a density of 2 × 10^6 cells per 100 μL. Cells were subcutaneously injected into nude mice. Five weeks after implantation, mice were sacrificed, and xenograft tumors were excised. Tumor volume was calculated as length × width² / 2.

Statistical analysis

Statistical analyses and data visualization were performed using R software (version 4.5.2) and GraphPad Prism (version 10). Comparisons between two independent groups were conducted using the Wilcoxon rank-sum test, whereas paired comparisons were performed using the Wilcoxon signed-rank test. Comparisons among three or more groups were conducted using the Kruskal-Wallis test. Fisher's exact test was used to compare categorical response distributions. P values were adjusted for multiple comparisons using the Benjamini-Hochberg method when applicable. Correlations between continuous variables were assessed using Spearman correlation analysis. Survival curves were generated using the Kaplan–Meier method and compared using the log-rank test. Cox proportional hazards regression analysis and time-dependent receiver operating characteristic (ROC) curve analysis were used for prognostic modeling and performance evaluation. A two-sided $P < 0.05$ was considered statistically significant unless otherwise specified.

Results

Palmitoylation-related molecular subtypes reveal biological and prognostic heterogeneity in PDAC

To characterize palmitoylation-associated molecular heterogeneity in PDAC, we performed unsupervised consensus clustering based on the expression of 34 palmitoylation-related genes in an integrated cohort of 145 patients from GSE62452 and GSE85916 (Additional file 1: Table S1). Evaluation of the consensus cumulative distribution function curve and the relative change in area under the curve supported k = 3 as the optimal clustering solution **(Figure S1A, B)**. Patients were classified into Cluster A (n = 54), Cluster B (n = 34), and Cluster C (n = 57) **(Fig. 2A; Additional file 1: Table S2)**. The consensus matrix showed high within-cluster consistency and clear separation among the three clusters, and principal component analysis further confirmed distinct transcriptomic distributions across the three subtypes **(Fig. 2B)**. Overall survival differed significantly among the subtypes, with Cluster B showing the shortest survival, Cluster C intermediate survival, and Cluster A the longest survival **(Fig. 2C)**. The 34 palmitoylation-related genes exhibited distinct cluster-associated expression patterns, with different gene subsets preferentially expressed across Clusters A, B and C **(Fig. 2D)**.

We next compared biological and microenvironmental features across the palmitoylation-related subtypes, focusing on Clusters A and B because they showed the greatest survival difference. Pathway enrichment analysis revealed greater enrichment of proliferative and DNA damage-repair programs in Cluster B, including DNA replication, mismatch repair, base excision repair, nucleotide excision repair,

and DNA damage-response pathways, while Cluster C generally showed intermediate enrichment of these pathways **(Fig. 2E)**. TME signature analysis showed higher scores for antigen-processing machinery, epithelial-mesenchymal transition, TMEscore, and TMEscoreA in Cluster B, whereas TMEscoreB was higher in Cluster A. ssGSEA-based immune profiling further showed broad immune remodeling in Cluster B, including higher enrichment of selected activated/memory T-cell, dendritic-cell, and natural killer-cell signatures, but lower enrichment of activated B-cell, mast-cell, effector memory CD8 + T-cell, and eosinophil signatures than Cluster A **(Figure S1C; Additional file 1: Table S3)**.

Pairwise differential-expression analyses identified 189 genes shared across all three subtype comparisons **(Fig. 2F; Additional file 1: Table S4)**. Among these genes, univariate Cox regression identified 25 genes significantly associated with overall survival **(Fig. 2G; Additional file 1: Table S5)**. Gene Ontology enrichment analysis linked these genes to cell-cycle regulation, chromosome organization, translation, oxidoreductase activity, and growth factor activity **(Fig. 2H)**. Based on these 25 prognosis-related genes, we calculated a patient-level palmitoylation score, termed PalS, using ssGSEA **(Additional file 1: Table S6)**. Patients in the PalS_High group had significantly shorter overall survival than those in the PalS_Low group in the integrated derivation cohort **(Fig. 2I)**. PalS largely recapitulated subtype-associated transcriptional differences, as most subtype-associated DEGs showed concordant changes in the PalS_High-versus-PalS_Low comparison. This concordance was weaker for Cluster C versus Cluster B, suggesting that PalS mainly reflected the transcriptional contrast between Clusters A and B and only partially captured Cluster C-related differences **(Figure S1D)**. Consistently, comparison of the 34 palmitoylation-related genes between the PalS_High and PalS_Low groups revealed distinct expression profiles, with several ZDHHC family members showing higher expression in the PalS_High group **(Figure S1E)**. Collectively, these findings indicate that palmitoylation-related molecular subtypes capture major biological, immune and prognostic heterogeneity in PDAC, and support the use of PalS as a patient-level measure of this subtype-associated transcriptional phenotype.

High PalS is associated with proliferative and immune-regulatory programs and unfavorable clinical outcomes

We next examined the relationship between PalS and the palmitoylation-related molecular subtypes. PalS differed significantly among the three subtypes, with the highest scores in Cluster B, the lowest scores in Cluster A, and intermediate scores in Cluster C **(Fig. 3A)**, consistent with the survival gradient observed across the three subtypes. A Sankey plot further showed that most Cluster B patients were classified into the PalS_High group, which contained a higher proportion of deaths, whereas Cluster A patients were predominantly assigned to the PalS_Low group and were more frequently alive **(Fig. 3B)**. A protein-protein interaction network based on genes differentially expressed between the PalS_High and PalS_Low groups revealed a densely connected integrin-associated adhesion module involving ITGA6, ITGB4, ITGB1, ITGA3, ITGA2, COL17A1, TNS4, and FLNB **(Fig. 3C)**. Hallmark gene-set analysis showed that PalS_High tumors had higher enrichment scores for several proliferation- and tumor progression-related programs, including mTORC1 signaling, MYC targets, G2/M checkpoint, E2F targets, glycolysis, and TGF-β signaling **(Fig. 3D)**. Immune-cell ssGSEA further revealed differences between the PalS

groups across activated and memory T-cell, regulatory T-cell, dendritic-cell, natural killer-cell, eosinophil, and B-cell signatures **(Fig. 3E)**. Several immune-regulatory genes, including CD274 and IDO1, together with genes involved in TGF-β signaling, were also expressed at higher levels in the PalS_High group **(Fig. 3F)**.

We further evaluated the clinical relevance of PalS in IMvigor210, an external cohort of patients with metastatic urothelial carcinoma treated with the anti-PD-L1 antibody atezolizumab[26]. Patients with complete or partial responses were classified as responders, whereas those with stable or progressive disease were classified as nonresponders. Nonresponders had significantly higher PalS scores than responders **(Fig. 3G)**. Patients in the PalS_High group also had significantly shorter overall survival than those in the PalS_Low group **(Fig. 3H)**, along with lower proportions of complete and partial responses and higher proportions of stable and progressive disease **(Fig. 3I)**. Collectively, high PalS was associated with proliferative and immune-regulatory programs in PDAC and with poorer response and survival in an external ICB-treated cohort.

Development and validation of a palmitoylation-associated prognostic signature in PDAC

Given the prognostic value of PalS, we developed a PalS-based prognostic signature for PDAC using the integrated GSE62452 and GSE85916 cohort as the training cohort. LASSO-penalized Cox regression identified a five-gene signature comprising FNDC3B, ALDH9A1, CAPRIN2, TTC9, and GPR133 **(Fig. 4A)**. The risk score was calculated as follows:

Risk score = − 0.3466 × ALDH9A1 + 0.2157 × FNDC3B + 0.1558 × CAPRIN2 + 0.1238 × TTC9 − 0.1626 × GPR133.

Kaplan–Meier analysis showed that patients in the high-risk group had significantly shorter overall survival than those in the low-risk group **(Fig. 4B)**. Time-dependent receiver operating characteristic analysis yielded area under the curve values of 0.659, 0.761, and 0.758 for 1-, 2-, and 3-year overall survival, respectively **(Fig. 4C)**. The model was further evaluated in the merged GSE57495 and GSE62452 datasets **(Fig. 4D)**, GSE62452 alone **(Fig. 4E)**, and TCGA-PAAD **(Fig. 4F)**. Across all validation cohorts, patients in the high-risk group had significantly shorter overall survival than those in the low-risk group. The 25 survival-associated candidate genes identified by univariate Cox regression showed distinct expression patterns between the high- and low-risk groups **(Fig. 4G)**. GSVA further revealed distinct pathway enrichment patterns between the two groups. The high-risk group showed increased enrichment of glycolysis, apical junction, mitotic spindle, hypoxia, p53 signaling, mTORC1 signaling, and G2/M checkpoint programs **(Fig. 4H)**. Together, these findings demonstrate that the five-gene signature captures prognostically distinct biological states in PDAC and provides a framework for identifying key functional regulators within the signature.

FNDC3B promotes PDAC cell growth, migration and tumorigenicity

We next evaluated the individual genes comprising the prognostic signature to identify candidates with potential biological relevance in PDAC. FNDC3B, CAPRIN2, and TTC9 showed higher expression in tumor tissues than in non-tumor tissues **(Figure S2A)**. Higher expression of FNDC3B, CAPRIN2, and TTC9 was associated with shorter overall survival, whereas higher expression of ALDH9A1 and GPR133 was associated with longer survival **(Figure S2B)**. These prognostic associations were further examined in an expanded GEO-TCGA meta-cohort comprising GSE21501, GSE62452, GSE85916, GSE57495, and TCGA-PAAD. High FNDC3B expression was significantly associated with shorter overall survival **(Fig. 5A)**, and the remaining four signature genes showed consistent survival associations **(Figure S2C)**. FNDC3B expression correlated with multiple palmitoylation-related genes, including positive correlations with ZDHHC5, ZDHHC7, ZDHHC9, ZDHHC20, and LYPLA1 **(Fig. 5B)**. These correlations were further evaluated in TCGA-PAAD and the expanded GEO-TCGA meta-cohort **(Figure S2D)**.

To determine the functional role of FNDC3B in PDAC cells, FNDC3B was knocked down in PANC-1 and PaTu8988 cells using two independent shRNAs. Western blotting confirmed efficient FNDC3B depletion in both cell lines **(Fig. 5C)**. FNDC3B knockdown impaired PDAC cell growth, as shown by reduced cell viability and growth in CCK-8 assays, with differences becoming more pronounced at later time points **(Fig. 5D, E)**. Consistently, colony formation assays showed significantly reduced clonogenic capacity after FNDC3B depletion in both cell lines **(Fig. 5F, G)**, and Transwell assays demonstrated significantly reduced PDAC cell migration **(Fig. 5H, I)**. Flow-cytometric analysis further revealed cell-line-dependent changes in cell-cycle distribution: FNDC3B knockdown reduced the G0/G1-phase fraction and increased the G2-phase population in PANC-1 cells, whereas it decreased the G2-phase population without significant changes in G0/G1 or S phase in PaTu8988 cells **(Fig. 5J, K)**. To explore transcriptional changes associated with FNDC3B depletion, we performed bulk RNA sequencing of control and FNDC3B-knockdown cells. Gene-set enrichment analysis revealed negative enrichment of mTOR-related signaling pathways following FNDC3B knockdown in both cell lines **(Figure S2E)**. Consistently, western blotting demonstrated reduced phosphorylation levels of mTOR, S6, and 4E-BP1 after FNDC3B depletion, whereas the corresponding total protein levels remained largely unchanged **(Fig. 5L)**. In xenograft models, representative excised tumors derived from FNDC3B-knockdown PANC-1 and PaTu8988 cells were smaller than those from control cells **(Fig. 5M)**, and endpoint tumor volume quantification confirmed significantly reduced tumor growth in both models following FNDC3B knockdown **(Fig. 5N)**.

Given the association of FNDC3B with the prognostic signature and its potential relevance to tumor biology, we next investigated whether FNDC3B was linked to immune features in PDAC. CIBERSORT analysis revealed substantial interpatient heterogeneity in inferred immune-cell composition (Figure S3A, B). Compared with the low-risk group, the high-risk group exhibited increased proportions of M0 macrophages and resting dendritic cells, together with reduced proportions of monocytes, naive B cells, and CD8 + T cells **(Figure S3C)**. Among the five signature genes, FNDC3B showed a positive correlation

with M0 macrophage abundance **(Figure S3D)**, and this association was consistently observed across four additional GEO-based cohorts **(Figure S3E)**.

Single-cell analysis identifies tumor-enriched FNDC3B-positive macrophages in PDAC

To place FNDC3B and palmitoylation-associated transcriptional activity within the cellular context of PDAC, we analyzed tumor-derived scRNA-seq data from six PDAC patients. After quality control, 28,291 high-quality cells were retained for downstream analysis **(Figure S4A-C)**. Seurat-based integration followed by UMAP visualization demonstrated effective inter-sample integration across the six samples **(Fig. 6A)**. Using canonical marker genes and established PDAC annotation strategies, we identified major cell populations, including T cells (CD2 and CD3D), fibroblasts (LUM), ductal cells (KRT19), macrophages (AIF1 and CD68), B cells (MS4A1), stellate cells (RGS5), endothelial cells (CDH5), mast cells (TPSAB1 and CPA3), neutrophils (S100A8 and G0S2), plasma cells (MZB1), and Schwann cells (S100B and GAP43) **(Fig. 6B)**. Cell-type composition analysis showed that T cells, fibroblasts, ductal cells, and macrophages were major components of the PDAC TME **(Fig. 6C)**.

At single-cell resolution, FNDC3B was detectable across multiple cellular compartments and showed relatively higher expression in fibroblasts, ductal cells, macrophages, endothelial cells, and neutrophils **(Fig. 6D, E)**. FNDC3B-positive cells were preferentially distributed within stromal, epithelial, and myeloid compartments, whereas T cells predominated among FNDC3B-negative cells **(Fig. 6F, G)**. Palmitoylation-associated transcriptional activity, assessed by AUCell scoring based on the palmitoylation-related gene set, was highest in ductal cells and fibroblasts, while macrophages, stellate cells, endothelial cells, and neutrophils showed intermediate scores **(Fig. 6H, I)**. Given the enrichment of FNDC3B expression within macrophages and their relevance to immune regulation, macrophages were selected for subsequent FNDC3B-centered analyses. Paired adjacent samples from the same six patients were incorporated for tumor-adjacent comparison. Tumor- and adjacent-derived cells occupied a shared integrated landscape **(Figure S4D)**. FNDC3B expression was increased and more broadly distributed in tumor-derived cells compared with adjacent-derived cells, as shown by UMAP visualization, violin plot analysis, and paired sample-level comparison **(Figure S4E-G)**. Consistently, the proportion of FNDC3B-positive macrophages was significantly increased in tumor samples compared with matched adjacent samples **(Figure S4H)**. Finally, an FNDC3B-positive macrophage signature derived from genes upregulated in FNDC3B-positive macrophages was projected onto the GSE62452-GSE85916 cohort. Patients with higher signature scores showed significantly worse overall survival than those with lower scores **(Figure S4I)**. Together, these findings support the association of tumor-enriched FNDC3B-positive macrophages with adverse prognosis in PDAC.

FNDC3B-positive macrophages exhibit an SPP1-centered communication program and localize to SPP1-rich tumor niches

Using the FNDC3B-based macrophage stratification defined in the Methods, we applied CellChat to infer ligand-receptor-mediated intercellular communication across annotated cell populations in the PDAC TME. The global CellChat network revealed extensive predicted interactions among epithelial, stromal, immune, and neural-associated populations **(Fig. 7A)**. Compared with FNDC3B-negative macrophages, FNDC3B-positive macrophages exhibited stronger outgoing signaling across multiple pathways, with SPP1 signaling showing the most prominent increase **(Fig. 7B)**. As sender cells, FNDC3B-positive macrophages displayed broad communication with multiple recipient populations **(Fig. 7C)**, and sender-specific networks for the remaining annotated populations supported this interconnected communication landscape **(Figure S5)**. Pathway-level analysis further linked FNDC3B-positive macrophages to several outgoing programs, including SPP1, FN1, MHC-related, COLLAGEN, and GALECTIN pathways, with SPP1 representing the dominant communication axis **(Fig. 7D)**. COLLAGEN and FN1 network analyses further showed matrix-associated communication patterns **(Figure S4J-M)**. SPP1 network analysis identified FNDC3B-positive macrophages as prominent senders of SPP1 signaling. Among ligand-receptor interactions, the SPP1-CD44 axis showed the largest contribution, followed by multiple SPP1-integrin interactions **(Fig. 7E)**. Bubble plots and circular network visualization further illustrated SPP1 signaling from FNDC3B-positive macrophages toward multiple recipient populations within the PDAC microenvironment **(Fig. 7F, G)**. Expression analysis supported the inferred SPP1 communication pattern: SPP1 was mainly enriched in macrophage populations, including FNDC3B-positive macrophages, whereas putative SPP1 receptors, including CD44 and integrin subunits, were broadly expressed across stromal, epithelial, endothelial, and immune compartments **(Fig. 7H, I)**. Within macrophages, joint stratification according to FNDC3B and SPP1 expression identified four macrophage states: FNDC3B-positive SPP1-positive, FNDC3B-positive SPP1-negative, FNDC3B-negative SPP1-positive, and double-negative macrophages **(Fig. 7J, K)**. These populations accounted for 56.4%, 16.6%, 14.9%, and 12.1% of macrophages, respectively, with FNDC3B-positive SPP1-positive macrophages representing the predominant state **(Fig. 7L)**.

To evaluate these single-cell and CellChat-derived findings at the tissue level, we performed multiplex immunofluorescence staining of paired PDAC tumor and peritumoral TMA cores. Composite and single-channel images demonstrated panCK, CD68, FNDC3B, SPP1, α-SMA, and DAPI signals across both tissue compartments **(Fig. 8A)**. Among FNDC3B-negative CD68-positive macrophages, the proportion of SPP1-positive cells was significantly higher in tumor tissues than in paired peritumoral tissues, whereas SPP1 positivity among FNDC3B-positive CD68-positive macrophages did not differ significantly between tissue compartments **(Fig. 8B)**. Within tumor tissues, FNDC3B-positive CD68-positive macrophages were more frequently localized within 30 μm of panCK-positive cells than FNDC3B-negative macrophages **(Fig. 8C)** and showed increased spatial proximity to SPP1-positive cells **(Fig. 8D)**. Enlarged multiplex images further illustrated FNDC3B and SPP1 signals within macrophage-rich regions **(Fig. 8E)**. Tumor-only analysis further demonstrated a higher proportion of SPP1-positive cells among FNDC3B-positive CD68-positive macrophages compared with FNDC3B-negative macrophages **(Fig. 8F)**. Across paired tissues, the proportions of FNDC3B-positive and SPP1-positive macrophages were positively correlated (Spearman $\rho = 0.473$) **(Fig. 8G)**. Collectively, these findings indicate that FNDC3B-positive

macrophages are associated with an enhanced SPP1-centered communication program and preferentially localize near tumor epithelial regions and SPP1-rich microenvironmental niches in PDAC.

Discussion

In this study, we used palmitoylation-related gene expression as a transcriptional entry point to characterize molecular heterogeneity in PDAC. This framework identified three palmitoylation-associated molecular subtypes with distinct survival outcomes, biological programs and immune microenvironmental features. We further derived a patient-level palmitoylation score and a five-gene prognostic model, and prioritized FNDC3B as a risk-associated candidate gene. By integrating functional experiments, single-cell analysis, CellChat inference and multiplex immunofluorescence, we linked FNDC3B to PDAC cell growth, mTOR-related signaling output and tumor-enriched macrophage niches characterized by SPP1-centered communication.

PDAC heterogeneity is shaped by both tumor-cell-intrinsic programs and the organization of the TME. Previous transcriptomic and multi-omic studies have classified PDAC into classical, basal-like/squamous and stroma-associated states with prognostic and therapeutic relevance[8–10]. In parallel, desmoplastic stroma and myeloid immune suppression are recognized as core features of the PDAC ecosystem[7, 12]. Our findings extend these classification efforts by showing that coordinated expression of palmitoylation-related genes can stratify PDAC patients into biologically and clinically distinct subtypes. Cluster B, which had the least favorable prognosis, showed enrichment of proliferative, DNA damage-repair, EMT and TME-remodeling programs, suggesting that palmitoylation-associated transcriptional patterns may mark an adverse tumor state integrating malignant epithelial activity and microenvironmental remodeling. This framework is biologically meaningful because S-palmitoylation is a reversible lipid modification that regulates membrane localization, protein trafficking, complex assembly and membrane-proximal signaling[15, 16]. These properties are directly relevant to cancer biology, where receptor signaling, adhesion, immune-regulatory molecules and ligand-receptor communication often depend on membrane dynamics. In PDAC, palmitoylation dysregulation has been linked to tumorigenesis, radiosensitivity, MYC-driven progression, metastasis, glycolytic activity and chemotherapy response[20–22, 45]. Most prior studies have focused on individual palmitoyltransferases, substrates or signaling axes. By contrast, our study captures palmitoylation-associated biology at the transcriptional program level and connects it with patient prognosis, pathway activity, immune infiltration and spatially resolved cellular states. Thus, the main value of this work is not the identification of a single biochemical palmitoylation event, but the construction of a clinically interpretable framework for studying palmitoylation-related heterogeneity in PDAC.

The palmitoylation score translated subtype-level differences into an individual-level measure. High PalS was associated with shorter survival and enrichment of proliferation, glycolysis, mTORC1, MYC/E2F and TGF-β-related programs, together with increased expression of immune-regulatory genes such as CD274 and IDO1. These findings suggest that high PalS reflects a proliferative and immune-regulatory tumor state. The association between high PalS and poorer outcome in the IMvigor210 immunotherapy-treated

cohort further supports the possibility that palmitoylation-associated transcriptional states intersect with immune-regulatory programs. Although this external cohort is not derived from PDAC, the analysis provides a useful exploratory link between PalS and therapy-associated clinical outcome. From a clinical modeling perspective, the five-gene signature consisting of FNDC3B, ALDH9A1, CAPRIN2, TTC9 and GPR133 provides a compact readout of palmitoylation-associated adverse biology. The model stratified patient survival and showed consistent prognostic performance across additional cohort settings. Compared with broad pathway scores or high-dimensional molecular classifications, a concise gene signature may be more amenable to future assay standardization and cohort-level validation. Therefore, this model may complement existing clinicopathological factors and transcriptomic subtype frameworks by providing a palmitoylation-associated risk dimension for PDAC prognostic assessment.

FNDC3B emerged as a particularly relevant candidate within this framework. It was upregulated in PDAC tumor tissues, associated with poor prognosis, correlated with macrophage infiltration and related to multiple palmitoylation-associated genes. Functionally, FNDC3B knockdown reduced PDAC cell proliferation, colony formation, migration and xenograft tumor growth. At the signaling level, FNDC3B depletion reduced phosphorylation of mTOR, S6 and 4E-BP1 while leaving total protein levels largely unchanged, suggesting attenuation of mTOR pathway activity rather than broad suppression of pathway protein abundance. Given the central role of mTOR signaling in nutrient sensing, protein synthesis, metabolic adaptation and PDAC progression[46, 47], FNDC3B may represent a candidate regulator linking transcriptional risk status with malignant tumor-cell behavior. Future studies clarifying the upstream intermediates between FNDC3B and mTOR activation may help define whether FNDC3B is a functional driver, pathway modulator or context-dependent marker of aggressive PDAC biology.

The single-cell and spatial analyses further broaden the relevance of FNDC3B from tumor-cell behavior to the immune microenvironment. FNDC3B expression was detected not only in epithelial compartments but also in fibroblasts and macrophages. FNDC3B-positive macrophages were enriched in tumor tissues, and their bulk-projected signature was associated with poor survival, suggesting that part of the FNDC3B-related risk signal may reflect a myeloid immune context. CellChat analysis associated FNDC3B-positive macrophages with enhanced outgoing communication, with SPP1 emerging as the dominant inferred signaling program. SPP1 can signal through CD44 and integrin receptors to regulate adhesion, migration, stromal remodeling and immune regulation[48], and previous studies have linked SPP1-positive macrophages to immune evasion and TME remodeling in pancreatic cancer[49–51]. Multiplex immunofluorescence provided spatial support for this inference by showing that FNDC3B-positive CD68-positive macrophages were enriched near panCK-positive tumor regions and SPP1-rich niches. These findings position FNDC3B-positive macrophages as a tumor-enriched myeloid state embedded in SPP1-associated tumor-stromal-immune communication networks.

This study also highlights several directions for future work. First, palmitoylation-associated transcriptional states should be integrated with direct palmitoyl-proteomic approaches to determine how transcriptional risk programs relate to biochemical S-palmitoylation events. Second, the five-gene model requires prospective validation in clinically annotated PDAC cohorts and comparison with established

clinicopathological and molecular classification systems. Third, the mechanistic relationship among FNDC3B, mTOR signaling and SPP1-associated macrophage niches warrants functional testing using rescue experiments, co-culture systems, ligand-receptor blockade and spatial omics. These studies will help determine whether FNDC3B is only a marker of aggressive tumor-microenvironmental states or an actionable regulator within this network.

In summary, this study delineates a palmitoylation-associated transcriptional framework for PDAC molecular stratification and prognostic assessment. Within this framework, FNDC3B links PDAC cell proliferation, migration, mTOR-related signaling and macrophage-enriched microenvironmental remodeling. These findings connect the dynamic biology of protein palmitoylation with tumor-cell malignant programs and spatial immune niches, providing a basis for future studies of PDAC risk stratification and microenvironment-focused intervention.

Abbreviations

PDAC
Pancreatic ductal adenocarcinoma
TME
Tumor microenvironment
PTMs
Post-translational modifications
GEO
Gene Expression Omnibus
TCGA
The Cancer Genome Atlas
GO
Gene Ontology
DEGs
Differentially expressed genes
ssGSEA
Single-sample gene set enrichment analysis
GSVA
Gene set variation analysis
LASSO
Least absolute shrinkage and selection operator
AUC
Area under the curve
ROC
Receiver operating characteristic
PCA
Principal component analysis

scRNA-seq
Single-cell RNA sequencing
UMAP
Uniform manifold approximation and projection
AUCell
Area under the curve-based scoring of gene sets in single cells
ICB
Immune checkpoint blockade
EMT
Epithelial–mesenchymal transition
TGF-β
Transforming growth factor-β
mTOR
Mechanistic target of rapamycin
CCK-8
Cell Counting Kit-8
TMA
Tissue microarray
mIF
Multiplex immunofluorescence

Declarations

Ethics approval and consent to participate

Ethics approval and consent to participate. All research procedures involving human participants were conducted in accordance with the Declaration of Helsinki. The study protocol was approved by the Research Ethics Committee of Peking University First Hospital (Ethical Review No. 2024 – 194) and the Institutional Animal Care and Use Committee of Peking University First Hospital (Ethical Review NO.S2025396).

Consent for publication

All authors agree to publish.

Competing interests

The authors declare that they have no competing interest for this work.

Funding

This study was supported by the National Key Research and Development Program of China (2023YFC2413400, 2023YFC2412401), the National Natural Science Foundation of China (82541012, 82571996, 82271764 and 82471772), the Beijing Natural Science Foundation (L246015), the National High Level Hospital Clinical Research Funding, including the Interdepartmental Research Project of Peking University First Hospital (2024IR11), Peking University Health Science Center-University of Michigan Joint Institute Clinical Translational Research Program (BMU2025JI002), Peking University Medicine plus X Pilot Program-Key Technologies R&D Project (BMU2024YXXLHGG008).

Author Contribution

JYL and EKZ designed the study and performed the majority of the experiments. JYL and EKZ analyzed and interpreted the data. WKL and GNL collected clinical samples and acquired clinical data. FSZ, CXZ, and YQD conducted statistical analysis and data validation. XDT, YMY, and YSM supervised the study and provided critical guidance. All authors read and approved the final manuscript.

Acknowledgements

Not available.

Data Availability

The datasets used and/or analyzed during the current study are available from the corresponding author upon reasonable request.

References

1. Siegel RL, et al. Cancer statistics, 2026. CA Cancer J Clin. 2026;76(1):e70043.
2. Roth S, et al. Pancreatic cancer. Nat Rev Dis Primers. 2026;12(1):23.
3. Stoop TF, et al. Pancreatic cancer. Lancet. 2025;405(10485):1182–202.
4. Hu ZI, O'Reilly EM. Therapeutic developments in pancreatic cancer. Nat Rev Gastroenterol Hepatol. 2024;21(1):7–24.
5. Farhangnia P, et al. Current and future immunotherapeutic approaches in pancreatic cancer treatment. J Hematol Oncol. 2024;17(1):40.
6. Leinwand J, Miller G. Regulation and modulation of antitumor immunity in pancreatic cancer. Nat Immunol. 2020;21(10):1152–9.

7. Ho WJ, Jaffee EM, Zheng L. The tumour microenvironment in pancreatic cancer - clinical challenges and opportunities. Nat Rev Clin Oncol. 2020;17(9):527–40.
8. Bailey P, et al. Genomic analyses identify molecular subtypes of pancreatic cancer. Nature. 2016;531(7592):47–52.
9. Moffitt RA, et al. Virtual microdissection identifies distinct tumor- and stroma-specific subtypes of pancreatic ductal adenocarcinoma. Nat Genet. 2015;47(10):1168–78.
10. Connor AA, Gallinger S. Pancreatic cancer evolution and heterogeneity: integrating omics and clinical data. Nat Rev Cancer. 2022;22(3):131–42.
11. Halbrook CJ, et al. Pancreatic cancer: Advances and challenges. Cell. 2023;186(8):1729–54.
12. Steele NG, et al. Multimodal Mapping of the Tumor and Peripheral Blood Immune Landscape in Human Pancreatic Cancer. Nat Cancer. 2020;1(11):1097–112.
13. Shakiba M, Tuveson DA. Macrophages and fibroblasts as regulators of the immune response in pancreatic cancer. Nat Immunol. 2025;26(5):678–91.
14. Pan S, Chen R. Pathological implication of protein post-translational modifications in cancer. Mol Aspects Med. 2022;86:101097.
15. Linder ME, Deschenes RJ. Palmitoylation: policing protein stability and traffic. Nat Rev Mol Cell Biol. 2007;8(1):74–84.
16. Mesquita FS, et al. Mechanisms and functions of protein S-acylation. Nat Rev Mol Cell Biol. 2024;25(6):488–509.
17. Tate EW, et al. Global profiling of protein lipidation using chemical proteomic technologies. Curr Opin Chem Biol. 2015;24:48–57.
18. Xu M, Xu B. Protein lipidation in the tumor microenvironment: enzymology, signaling pathways, and therapeutics. Mol Cancer. 2025;24(1):138.
19. Song P, et al. Palmitic acid and palmitoylation in cancer: Understanding, insights, and challenges. Innov (Camb). 2025;6(8):100918.
20. Wang Y, et al. SMAD4 Palmitoylation Drives a Metabolic-Transcriptional Circuit to Promote Tumorigenesis and Confers Radiosensitivity in Pancreatic Cancer. Adv Sci (Weinh). 2026;13(41):e19791.
21. Zhang H, et al. ZDHHC20-mediated S-palmitoylation of YTHDF3 stabilizes MYC mRNA to promote pancreatic cancer progression. Nat Commun. 2024;15(1):4642.
22. Chen L, et al. Palmitoylation alters LDHA activity and pancreatic cancer response to chemotherapy. Cancer Lett. 2024;587:216696.
23. Zhang Y et al. ABHD17C-Mediated S-Depalmitoylation of BCL6B Enhances CD24 Transcription to Resist Macrophage Phagocytosis in Pancreatic Cancer. Adv Sci (Weinh), 2026: p. e75757.
24. Edgar R, Domrachev M, Lash AE. *Gene Expression Omnibus: NCBI gene expression and hybridization array data repository.* Nucleic Acids Res, 2002. 30(1): pp. 207 – 10.

25. The Cancer Genome Atlas Research Network. Integrated Genomic Characterization of Pancreatic Ductal Adenocarcinoma. Cancer Cell. 2017;32(2):185–e20313.
26. Mariathasan S, et al. TGFβ attenuates tumour response to PD-L1 blockade by contributing to exclusion of T cells. Nature. 2018;554(7693):544–8.
27. Ritchie ME, et al. limma powers differential expression analyses for RNA-sequencing and microarray studies. Nucleic Acids Res. 2015;43(7):e47.
28. Johnson WE, Li C, Rabinovic A. Adjusting batch effects in microarray expression data using empirical Bayes methods. Biostatistics. 2007;8(1):118–27.
29. Liberzon A, et al. Molecular signatures database (MSigDB) 3.0. Bioinformatics. 2011;27(12):1739–40.
30. Ashburner M, et al. Gene ontology: tool for the unification of biology. The Gene Ontology Consortium. Nat Genet. 2000;25(1):25–9.
31. Wilkerson MD, Hayes DN. ConsensusClusterPlus: a class discovery tool with confidence assessments and item tracking. Bioinformatics. 2010;26(12):1572–3.
32. Barbie DA, et al. Systematic RNA interference reveals that oncogenic KRAS-driven cancers require TBK1. Nature. 2009;462(7269):108–12.
33. Hänzelmann S, Castelo R, Guinney J. GSVA: gene set variation analysis for microarray and RNA-seq data. BMC Bioinformatics. 2013;14:7.
34. Simon N, et al. Regularization Paths for Cox's Proportional Hazards Model via Coordinate Descent. J Stat Softw. 2011;39(5):1–13.
35. Blanche P, Dartigues JF, Jacqmin-Gadda H. Estimating and comparing time-dependent areas under receiver operating characteristic curves for censored event times with competing risks. Stat Med. 2013;32(30):5381–97.
36. Yu G, et al. clusterProfiler: an R package for comparing biological themes among gene clusters. Omics. 2012;16(5):284–7.
37. Newman AM, et al. Robust enumeration of cell subsets from tissue expression profiles. Nat Methods. 2015;12(5):453–7.
38. Chen K, et al. Immune profiling and prognostic model of pancreatic cancer using quantitative pathology and single-cell RNA sequencing. J Transl Med. 2023;21(1):210.
39. Stuart T, et al. Comprehensive Integration of Single-Cell Data. Cell. 2019;177(7):1888. –1902.e21.
40. Becht E, et al. Dimensionality reduction for visualizing single-cell data using UMAP. Nat Biotechnol. 2019;37(1):38–44.
41. Aibar S, et al. SCENIC: single-cell regulatory network inference and clustering. Nat Methods. 2017;14(11):1083–6.
42. Jin S, et al. Inference and analysis of cell-cell communication using CellChat. Nat Commun. 2021;12(1):1088.

43. Bankhead P, et al. QuPath: Open source software for digital pathology image analysis. Sci Rep. 2017;7(1):16878.
44. Pachitariu M, Rariden M, Stringer C. *Cellpose-SAM: superhuman generalization for cellular segmentation.* bioRxiv, 2025.
45. Tomić G, et al. Palmitoyl transferase ZDHHC20 promotes pancreatic cancer metastasis. Cell Rep. 2024;43(5):114224.
46. Saxton RA, Sabatini DM. mTOR Signaling in Growth, Metabolism, and Disease. Cell. 2017;168(6):960–76.
47. Rozengurt E, Eibl G. Pancreatic cancer: molecular pathogenesis and emerging therapeutic strategies. Signal Transduct Target Ther. 2026;11(1):6.
48. Gu Y, Muller WJ. The Multifaceted Role of Osteopontin in Modulating the Tumor Microenvironment. Cancer Res. 2025;85(21):4049–61.
49. Klement JD, et al. An osteopontin/CD44 immune checkpoint controls CD8 + T cell activation and tumor immune evasion. J Clin Invest. 2018;128(12):5549–60.
50. Li H, et al. SPP1 is required for maintaining mesenchymal cell fate in pancreatic cancer. Nature. 2025;648(8092):203–9.
51. Li E, Cheung HCZ, Ma S. CTHRC1(+) fibroblasts and SPP1(+) macrophages synergistically contribute to pro-tumorigenic tumor microenvironment in pancreatic ductal adenocarcinoma. Sci Rep. 2024;14(1):17412.

Figures

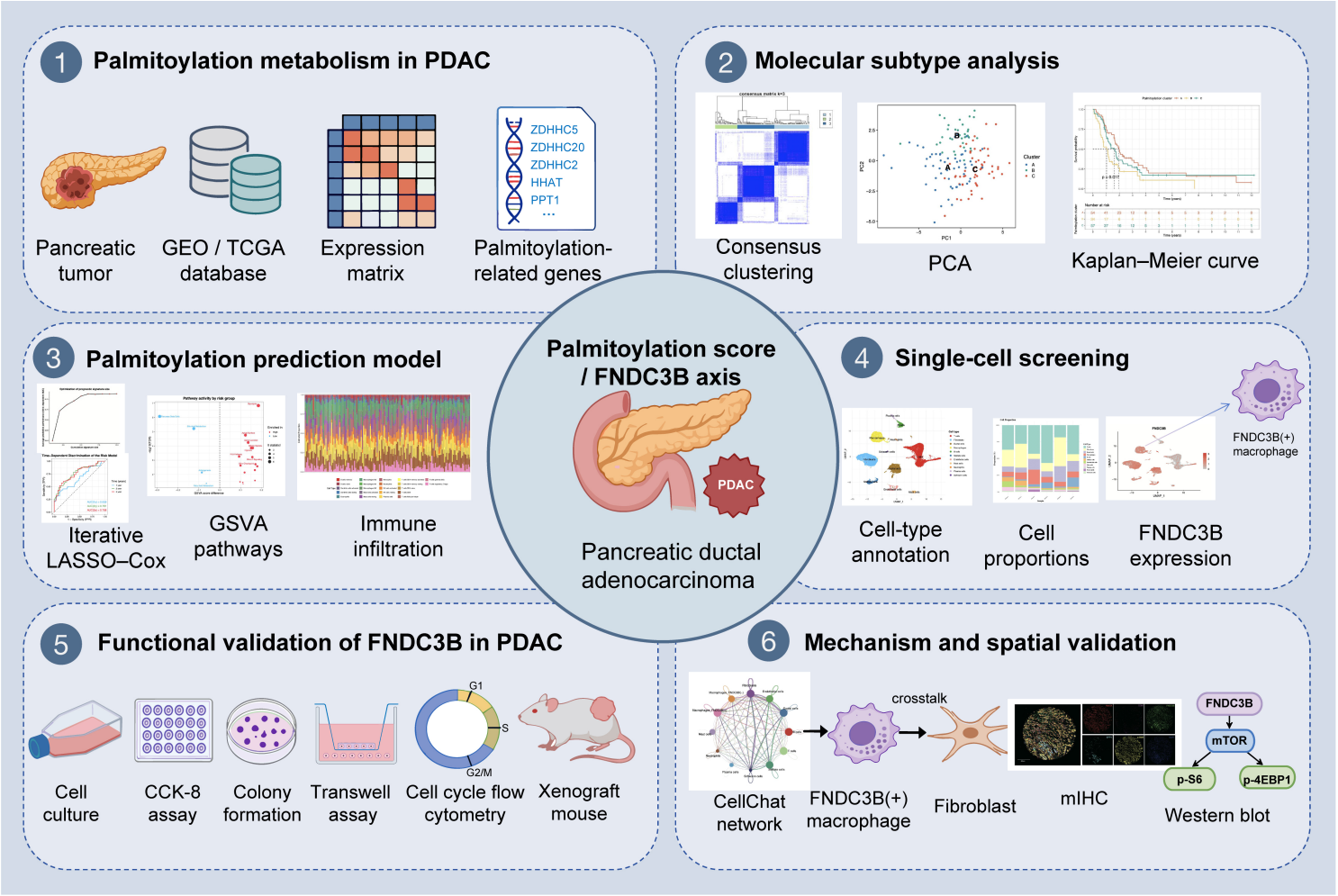


Figure 1

Workflow diagram illustrating the study design and analytical pipeline.

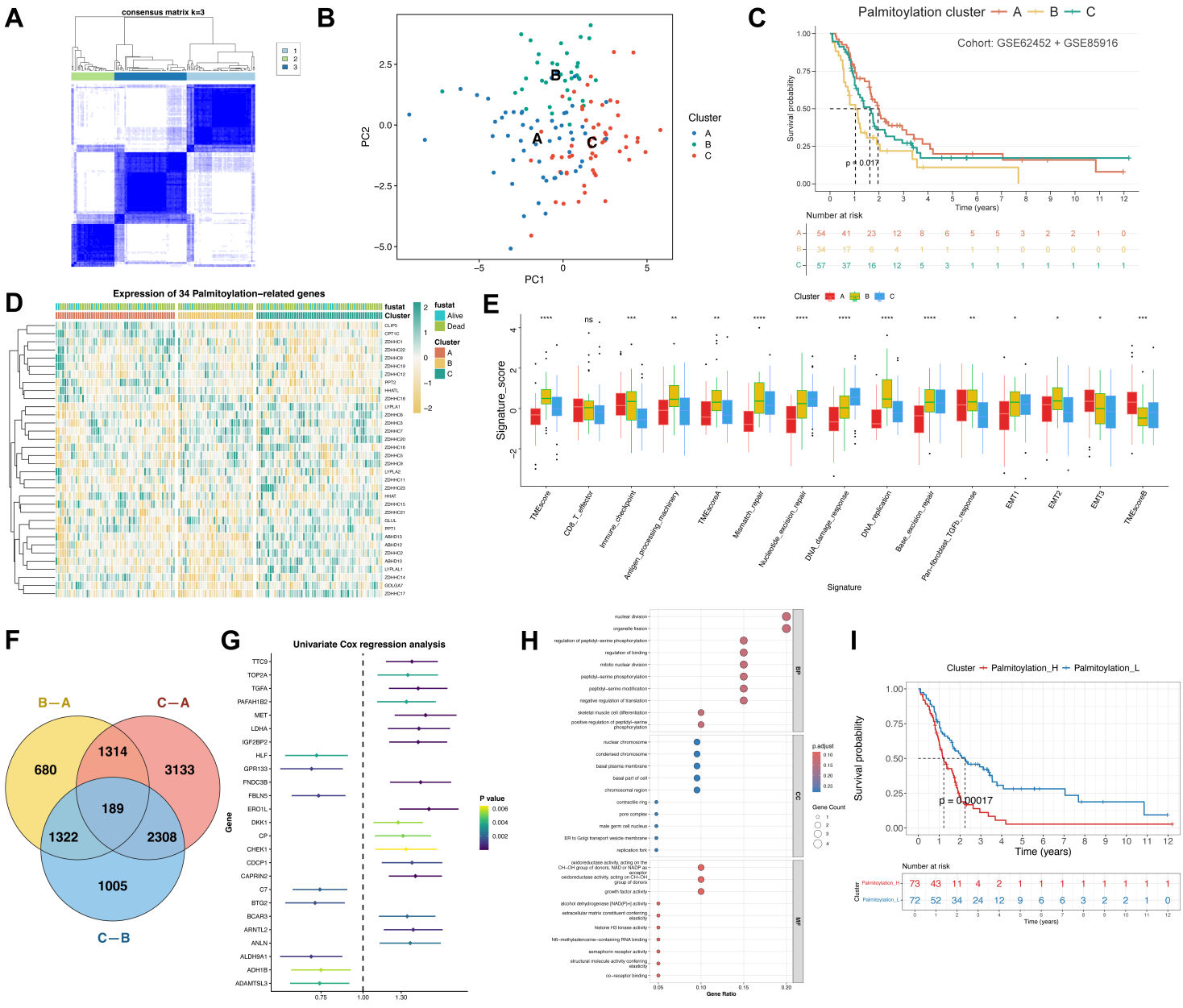


Figure 2

(A) Consensus clustering matrix of the integrated GEO cohort based on 34 palmitoylation-related genes, identifying Cluster A, Cluster B and Cluster C. (B) Principal component analysis (PCA) of the three palmitoylation-related clusters. (C) Kaplan–Meier analysis of overall survival among the three clusters (P = 0.017). (D) Heatmap showing expression patterns of palmitoylation-related genes across the three clusters. (E) Gene-set enrichment analysis of proliferative and DNA damage-repair pathways across the three palmitoylation-related molecular subtypes. (F) Venn diagram of overlapping differentially expressed genes (DEGs) across the three molecular subtypes. (G) Forest plot of prognosis-related genes identified by univariate Cox regression analysis. (H) GO enrichment of prognosis-associated overlapping genes. (I) Kaplan–Meier survival analysis of the PalS_High and PalS_Low groups in the integrated derivation cohort. (*P < 0.05; **P < 0.01; ***P < 0.001.)

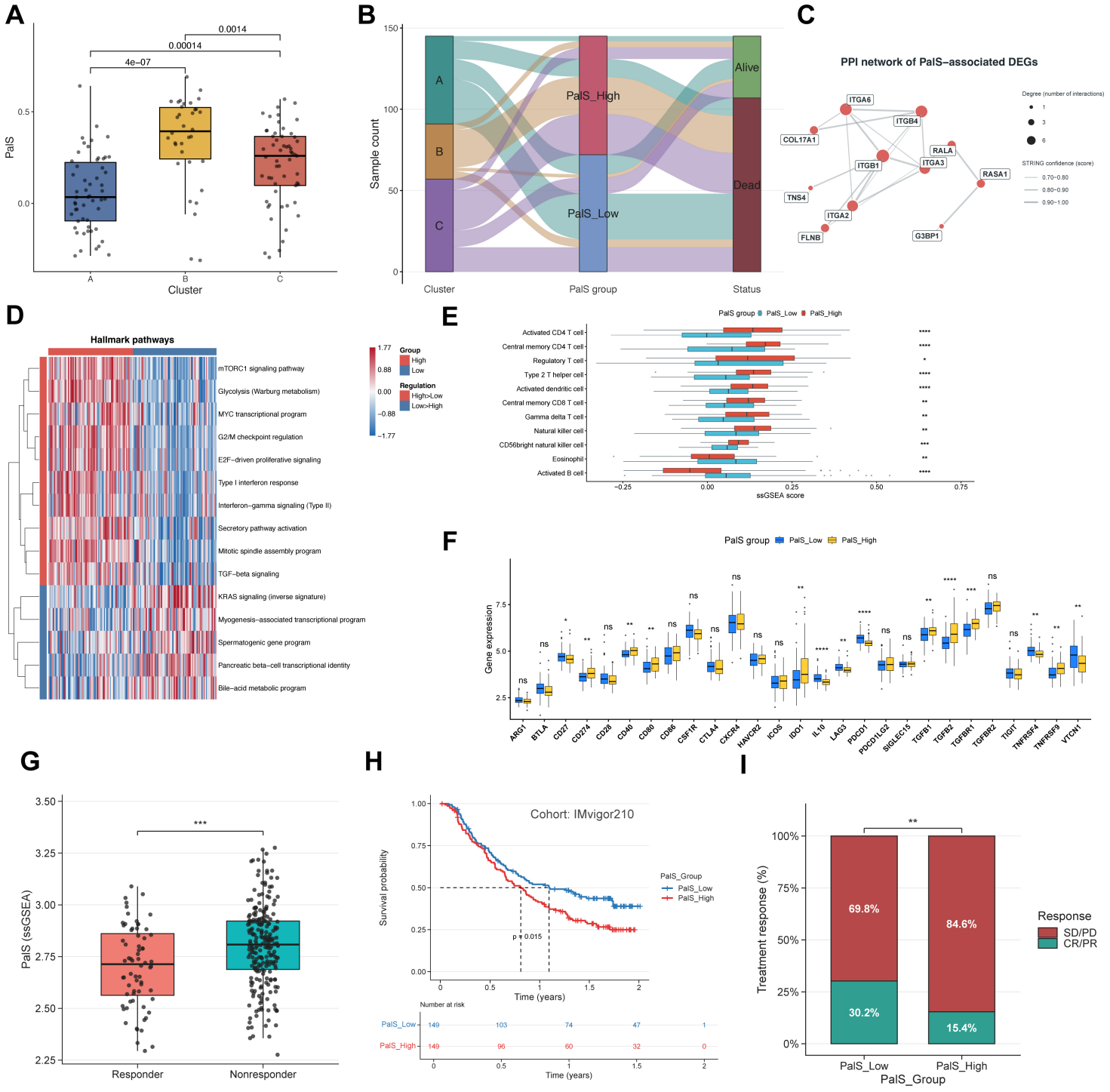


Figure 3

(A) Distribution of PalS across the three palmitoylation-related molecular subtypes. (B) Sankey diagram linking molecular subtype, PalS group and vital status at the last follow-up. (C) Protein–protein interaction network constructed from genes differentially expressed between the PalS_High and PalS_Low groups. (D) Hallmark gene-set enrichment analysis of biological pathways in the PalS_High and PalS_Low groups. (E) ssGSEA-based comparison of immune-cell-associated signatures between the PalS_High and PalS_Low groups. (F) Expression of representative immune-regulatory genes in the

PalS_High and PalS_Low groups. (G) PalS in responders and nonresponders in the IMvigor210 cohort. (H) Kaplan–Meier analysis of the PalS_High and PalS_Low groups in the IMvigor210 cohort. (I) Distribution of immunotherapy response categories between the PalS_High and PalS_Low groups. (*P < 0.05; **P < 0.01; ***P < 0.001.)

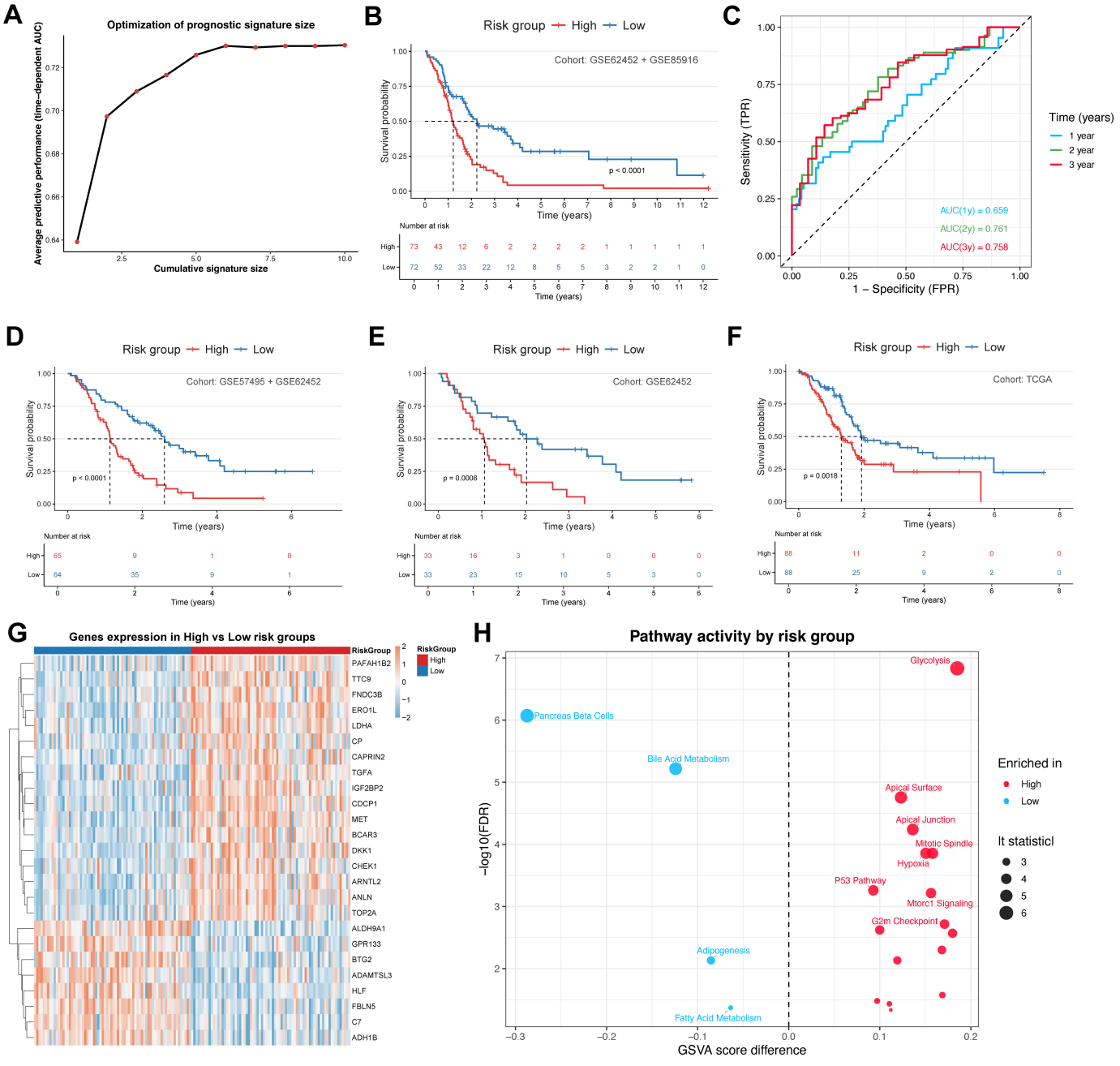


Figure 4

(A) Iterative LASSO-Cox optimization showing the mean time-dependent AUC across cumulative top-frequency genes. The five-gene signature was retained as a parsimonious model after the AUC curve reached a plateau. (B) Kaplan–Meier analysis of high- and low-risk groups in the training cohort. (C)

Time-dependent ROC curves for 1-, 2- and 3-year overall survival prediction. (D–F) Kaplan–Meier performance assessment in the merged GSE57495-GSE62452 dataset, GSE62452, and TCGA-PAAD. (G) Heatmap illustrating the expression patterns of the 25 survival-associated candidate genes between the high- and low-risk groups. (H) GSVA of biological pathways between the high- and low-risk groups.

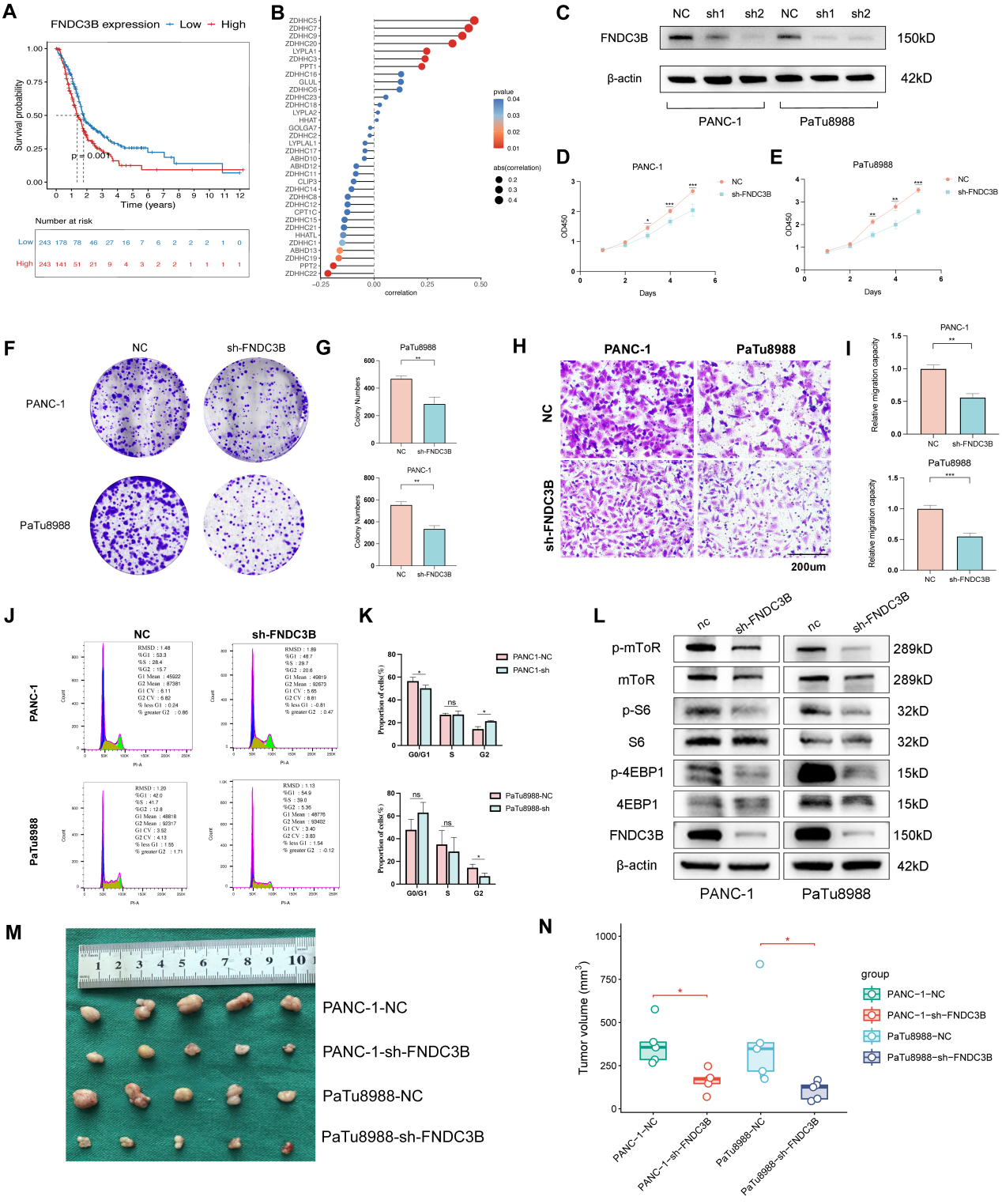


Figure 5

(A) Kaplan–Meier analysis of FNDC3B expression in the expanded GEO–TCGA meta-cohort. (B) Correlation analysis between FNDC3B and palmitoylation-related genes. (C) Western blot validation of FNDC3B knockdown in PANC-1 and PaTu8988 cells. (D, E) CCK-8 assays showing reduced cell viability and growth after FNDC3B knockdown in PANC-1 and PaTu8988 cells. (F, G) Colony formation assays showing impaired clonogenic growth following FNDC3B knockdown in PANC-1 and PaTu8988 cells. (H, I) Transwell migration assays showing decreased migratory ability in FNDC3B-knockdown PANC-1 and PaTu8988 cells. Magnification: 200×. (J, K) Flow-cytometric analysis of cell-cycle distribution after FNDC3B knockdown in PANC-1 and PaTu8988 cells. (L) Western blot analysis showing reduced phosphorylation of mTOR, S6 and 4E-BP1 after FNDC3B knockdown. (M) Representative xenograft tumors derived from control and FNDC3B-knockdown PANC-1 and PaTu8988 cells. (N) Endpoint quantification of xenograft tumor volumes in control and FNDC3B-knockdown groups. (*P < 0.05; **P < 0.01; ***P < 0.001; ****P < 0.0001.)

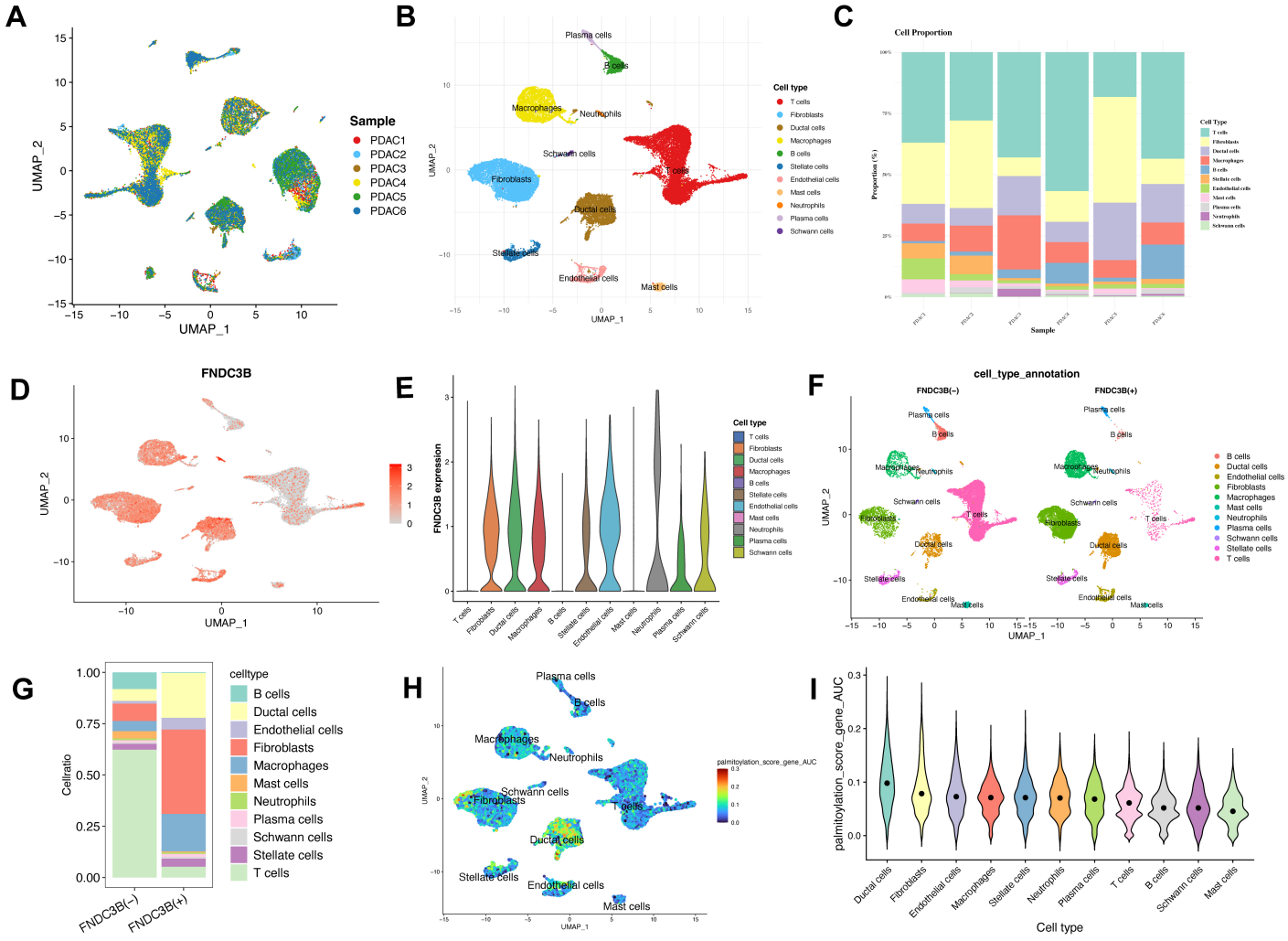


Figure 6

(A) Integrated UMAP visualization of tumor-derived scRNA-seq data from six PDAC patients. (B) UMAP of major annotated cell populations in the PDAC TME. (C) Cell-type composition across the six tumor-derived samples. (D, E) FNDC3B expression across the single-cell landscape and annotated cell types. (F, G) Distribution and cell-type composition of FNDC3B-positive and FNDC3B-negative cells. (H, I) Palmitoylation-related AUCell activity across the single-cell landscape and major cell populations.

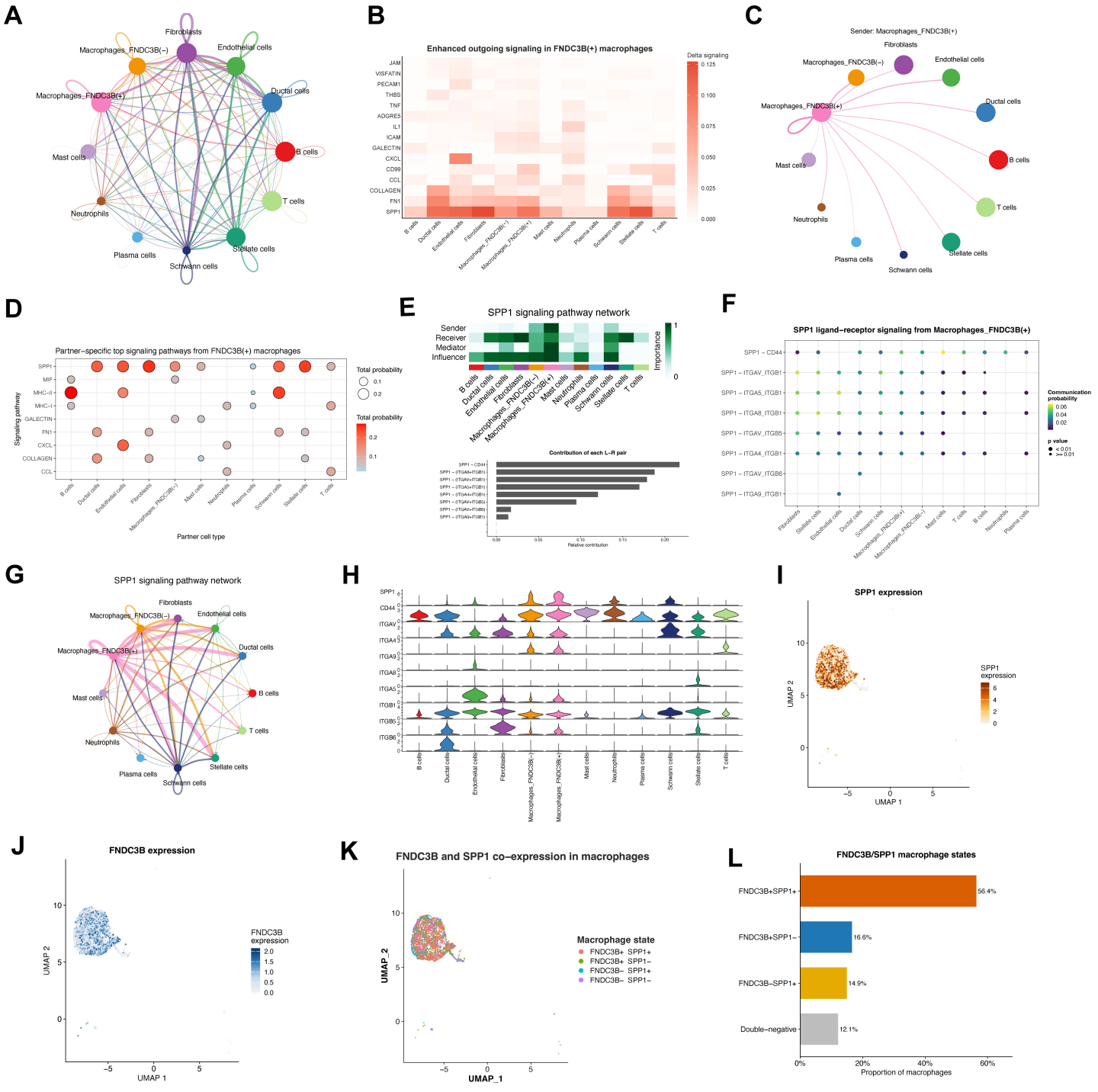


Figure 7

(A) Global CellChat-inferred communication network across annotated cell populations. (B) Enhanced outgoing signaling pathways in FNDC3B-positive macrophages compared with FNDC3B-negative macrophages. (C) Outgoing communication network from FNDC3B-positive macrophages to recipient cell populations. (D) Pathway-level outgoing signaling patterns associated with FNDC3B-positive macrophages. (E) Network role and ligand–receptor contribution of the SPP1 signaling pathway. (F, G) Bubble plot and circular network of SPP1-mediated communication from FNDC3B-positive macrophages. (H, I) Expression of SPP1 and its major receptors across annotated cell populations. (J, K) Joint stratification of macrophages according to FNDC3B and SPP1 expression. (L) Quantification of FNDC3B/SPP1-defined macrophage subsets.

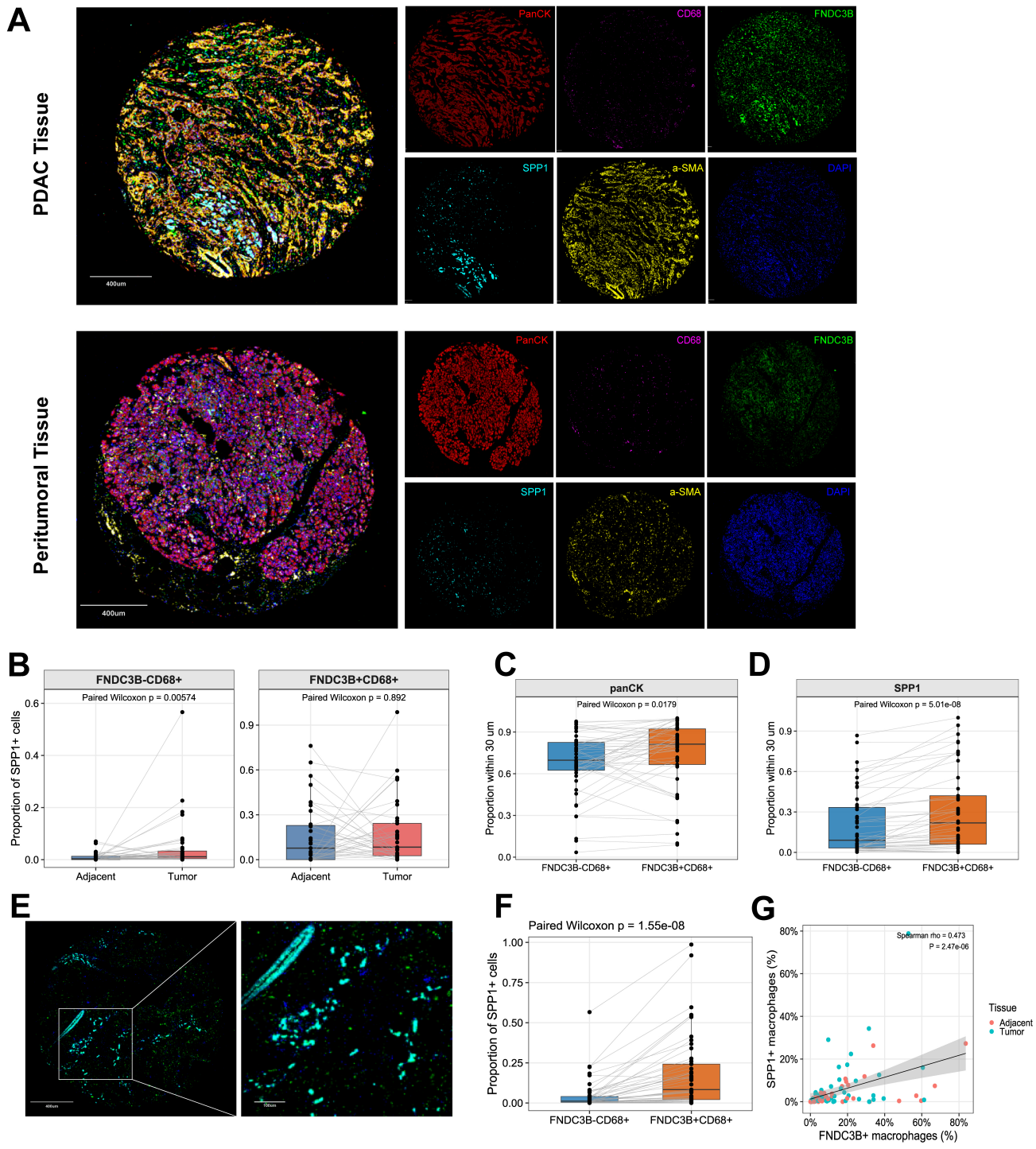


Figure 8

(A) Representative composite and single-channel multiplex immunofluorescence images of paired PDAC tumor and peritumoral TMA cores stained for panCK, CD68, FNDC3B, SPP1, α-SMA and DAPI. (B) SPP1-positive proportions within FNDC3B-negative and FNDC3B-positive CD68-positive macrophages in paired tumor and peritumoral tissues. (C) Proportions of FNDC3B-positive and FNDC3B-negative CD68-positive macrophages located within 30 μm of panCK-positive epithelial/tumor cells. (D) Proportions of FNDC3B-

positive and FNDC3B-negative CD68-positive macrophages located within 30 μm of SPP1-positive cells. (E) Enlarged multiplex immunofluorescence images showing FNDC3B and SPP1 signals in macrophage-rich regions. (F) Tumor-only comparison of SPP1 positivity between FNDC3B-positive and FNDC3B-negative CD68-positive macrophages. (G) Correlation between FNDC3B-positive and SPP1-positive macrophage proportions across paired tissues. (*P < 0.05; **P < 0.01; ***P < 0.001.)

Supplementary Files

This is a list of supplementary files associated with this preprint. Click to download.

- FigureS1.jpg
- FigureS2.jpg
- FigureS3.jpg
- FigureS4.jpg
- FigureS5.jpg
- SupplementaryTables.xlsx
- SupplementaryUncroppedWesternBlotImages.pdf